

Cite this: *J. Mater. Chem.*, 2012, **22**, 7537

www.rsc.org/materials

PAPER

## Hierarchically porous LiFePO<sub>4</sub>/nitrogen-doped carbon nanotubes composite as a cathode for lithium ion batteries†

Jinli Yang,<sup>a</sup> Jiajun Wang,<sup>a</sup> Xifei Li,<sup>a</sup> Dongniu Wang,<sup>a</sup> Jian Liu,<sup>a</sup> Guoxian Liang,<sup>b</sup> Michel Gauthier,<sup>b</sup> Yongliang Li,<sup>a</sup> Dongsheng Geng,<sup>a</sup> Ruying Li<sup>a</sup> and Xueliang Sun<sup>\*a</sup>

Received 18th January 2012, Accepted 6th February 2012

DOI: 10.1039/c2jm30380a

A porous composite of LiFePO<sub>4</sub>/nitrogen-doped carbon nanotubes (N-CNTs) with hierarchical structure was prepared by a sol-gel method without templates or surfactants. Highly conductive and uniformly dispersed N-CNTs incorporated into three dimensional interlaced porous LiFePO<sub>4</sub> can facilitate the electronic and lithium ion diffusion rate. The LiFePO<sub>4</sub>/N-CNTs composites deliver a reversible discharge capacity of 138 mA h g<sup>-1</sup> at a current density of 17 mA g<sup>-1</sup> while the LiFePO<sub>4</sub>/CNTs composites only deliver 113 mA h g<sup>-1</sup>, demonstrating N-CNTs modified composites can act as a promising cathode for high-performance lithium-ion batteries.

### 1. Introduction

The past few years have witnessed an unprecedented increase of interest in large scale batteries demand for energy storage to develop electric vehicles (EVs) and hybrid electric vehicles (HEVs).<sup>1-5</sup> Since the pioneer work of Goodenough and co-workers,<sup>6</sup> LiFePO<sub>4</sub> has become a promising material for large size lithium-ion batteries due to its low cost, environmental compatibility, high theoretical specific capacity of 170 mA h g<sup>-1</sup> and especially a superior safety performance. Unfortunately, one of the main obstacles of LiFePO<sub>4</sub> for its practical applications is its poor rate capability, which can be attributed to sluggish kinetics of lithium-ion diffusion through the LiFePO<sub>4</sub>-FePO<sub>4</sub> interfaces and the poor electronic conductivity.<sup>7,8</sup>

The kinetics of the lithium ion extraction/insertion process can be facilitated by reducing the particle size,<sup>9,10</sup> doping with iso-valent ions,<sup>11,12</sup> or coating with a conductive carbon layer.<sup>13-15</sup> Decreasing the size of the LiFePO<sub>4</sub> crystallites to nanosize can shorten the lithium ion diffusion pathway and improve its rate capacity, but the nano-sized LiFePO<sub>4</sub> material is usually accompanied by low tap density and a low volumetric capacity in practical battery application.<sup>16</sup> For introducing guest atoms into the crystal lattices of LiFePO<sub>4</sub>, there is still much debate about the precise substitution mechanisms and whether the considerable increase in electronic conductivity is from the doping effect or carbon contamination.<sup>17</sup> Therefore, addition or coating with conductive carbon is the most widely used technique in

improvement of electronic conductivity and rate performance of LiFePO<sub>4</sub>.

Nevertheless, the simple carbon coating or additive cannot achieve an ideal rate performance especially for micro-sized LiFePO<sub>4</sub>. Also, the charge distribution is not homogeneous in the perpendicular direction to the electrode surface at high charge/discharge rate for the bulk LiFePO<sub>4</sub> material, which results in lower efficiency of the active material.<sup>18</sup> Although nanosized LiFePO<sub>4</sub> may improve the homogeneity of carbon distribution, the low tap density is still a big challenge for the requirement of high volume energy density in EVs applications. Therefore a balance between the tap density and homogeneous conductive carbon distribution should be considered carefully and developing novel structured LiFePO<sub>4</sub> such as three dimensional (3D) porous LiFePO<sub>4</sub> architectures is a feasible strategy because it achieves fast electronic and ion conduction, while keeping an acceptable tap density.<sup>16</sup> In addition, the porous strategy also allows efficient percolation of the electrolyte through the electrode, favoring the electrolyte access to active material *via* the pores, then make efficient use of electrode material.<sup>19-21</sup>

Doherty *et al.*<sup>22</sup> successfully prepared porous LiFePO<sub>4</sub>-carbon composites by using a template method, which exhibited 100 mA h g<sup>-1</sup> at a high discharge rate of 5 C. Considering the importance of carbon in the composite, the choice of a more appropriate carbon material such as carbon nanotubes (CNTs) is important for high-performance of the composite. Zhou *et al.*<sup>23</sup> combined the advantages of porous LiFePO<sub>4</sub> and carbon nanotubes (CNTs) and developed LiFePO<sub>4</sub>/CNT composites, yielding a high-performance cathode material for high-energy density and high-power density lithium-ion batteries. However, the CNTs were not quite uniformly dispersed in the modified composite, which leads to ineffective transfer of the electrons. Therefore, to make full use of the CNTs conductive network, uniform CNTs dispersion in the LiFePO<sub>4</sub> composite is critical.

<sup>a</sup>Department of Mechanical and Materials Engineering, The University of Western Ontario, ON, Canada N6A 5B9. E-mail: xsun@eng.uwo.ca; Fax: +1-519-661-3020; Tel: +1-519-661-2111 ext. 87759

<sup>b</sup>Phostech Lithium Inc., 1475, rue Marie-Victorin, St-Bruno, QC, Canada J3V 6B7

† Electronic supplementary information (ESI) available: Cross-sectional SEM image and EDS mapping. See DOI: 10.1039/c2jm30380a

It is widely accepted that nitrogen doped carbon nanotubes (N-CNTs) possess many active defects and hydrophilic properties, allowing more uniform dispersion of N-CNTs into porous  $\text{LiFePO}_4$  and leading to intimate contact with active material. In addition, N-CNTs could further enhance the electronic conductivity because the additional electrons contributed by the nitrogen atom provide electron carriers for the conduction band.<sup>24–26</sup> Herein, we present 3D N-CNTs modified porous  $\text{LiFePO}_4$  (LFP/N-CNTs) obtained by a sol–gel approach combined with high-temperature calcinations. In particular, compared with the CNTs modified  $\text{LiFePO}_4$  composites (LFP/CNTs) and the pristine porous  $\text{LiFePO}_4$  (LFP), significant effects of the N-CNTs on the electrochemical performance of porous  $\text{LiFePO}_4$  were revealed. The possible mechanisms were also discussed and elucidated.

## 2. Experimental

### 2.1 Synthesis of $\text{LiFePO}_4$ and $\text{LiFePO}_4$ composite

Multiwalled carbon nanotubes (CNTs) purchased from Shenzhen Nanotech Port Co. Ltd. were used in this study. The diameter of CNTs is in the range of 40 to 60 nm. Nitrogen doped carbon nanotubes (N-CNTs) with similar diameter range were prepared by ultrasonic spray pyrolysis reported previously.<sup>25</sup>

*In situ* sol–gel experiments were conducted in aqueous solution under ambient atmosphere. In a typical synthesis, LFP/N-CNTs and LFP/CNTs composites were prepared by using an *in situ* sol–gel method as follows: first 80 mg N-CNTs were dispersed in 30 mL of water *via* strong ultrasonic agitation for 30 min, then 1.039 g lithium dihydrogen phosphate ( $\text{LiH}_2\text{PO}_4$ ) was dissolved in 100 mL of water and stirred at 80 °C for 1 h. Separately, 2.449 g iron(III) citrate ( $\text{FeC}_6\text{H}_5\text{O}_7$ ) was dissolved in 70 mL of water by stirring at 70 °C for 1 h. The three solutions were mixed together and dried at 70 °C for 24 h. After thorough grinding with a mortar and pestle, the obtained material was fired in an inert (argon) atmosphere at 700 °C for 10 h with a heating rate of 10 °C  $\text{min}^{-1}$ . The synthesis procedure of LFP/CNTs was the same as above. For LFP, all the experimental parameters were kept the same as above except without the addition of N-CNTs or CNTs.

### 2.2 Physical characterization

The XRD analysis was performed on a Rigaku rotating-anode X-ray Diffractometer. The diffractometer employs  $\text{Co K}\alpha$  radiation, with monochromation being achieved using a curved crystal, diffracted beam and graphite monochromator. The instrument was operated at 45 kV and 160 mA. The experimental diffraction patterns were completed from 2 to 82° two-theta, at a rate of 10 degrees per minute.

Scanning electron microscopy (SEM) images were taken on a Hitachi S-4800 microscope, operating at 5 kV. TEM measurements were carried out with a Hitachi H-7000 transmission electron microscopy (TEM). Raman scattering (RS) spectra were recorded on a HORIBA Scientific LabRAM HR Raman spectrometer system equipped with a 532.4 nm laser.  $\text{N}_2$  adsorption/desorption isotherms were performed using a Folio Micromeritics TriStar II Surface Area and Pore Size Analyser.

## 2.3 Electrochemical measurements

The electrochemical performances were carried out using a computer-controlled Arbin BT-2000 Battery Test Station with coin-shape half cells between 2.5 and 4.2 V at different rates. The electrolyte was 1 M  $\text{LiPF}_6$  solution in a 1 : 1 mixture of ethylene carbonate (EC) and dimethyl carbonate (DMC). The working electrode was fabricated by mixing the active material ( $\text{LiFePO}_4$ )/acetylene black/polyvinylidene fluoride with a weight ratio of 75 : 15 : 10, then grinding the mixture in a mortar and pestle. The resultant slurry, pasted on Al foil, was dried at 100 °C under vacuum for 24 h. The coin cells (2352) were assembled in a high purity argon filled glove box.

Charge–discharge testing was conducted galvanostatically at different C rates within the voltage range of 2.5–4.2 V (*vs.*  $\text{Li}^+/\text{Li}$ ). Cyclic voltammogram (CV) measurements were performed on an electrochemical workstation (potentiostat/galvanostat/EIS (VMP3)) over the potential range 2.5–4.2 V *vs.*  $\text{Li}^+/\text{Li}$  at a scanning rate of 0.1  $\text{mV s}^{-1}$ . All the electrochemical measurements were conducted at room temperature.

The conductivity was measured on a home-made device by compacting powders in a 4 mm inner diameter quartz tube under a 40 psi pressure.

## 3. Results and discussion

Typical scanning electron microscopy (SEM) and transmission electron microscopy (TEM) images of CNTs and N-CNTs are shown in Fig. 1. From low magnification micrographs (Fig. 1a and c), both CNTs and N-CNTs have the similar length ranging from 25 to 30 micrometres. A high magnification (Fig. 1b and d) reveals both CNTs and N-CNTs have the similar average

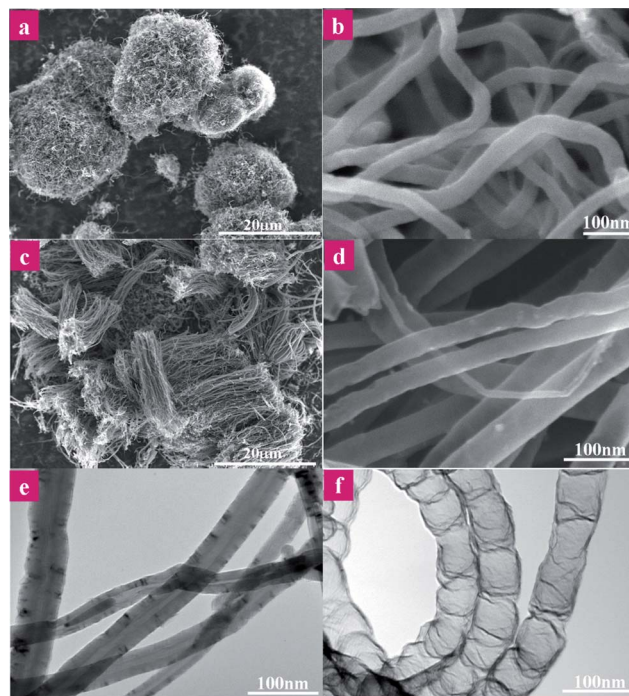


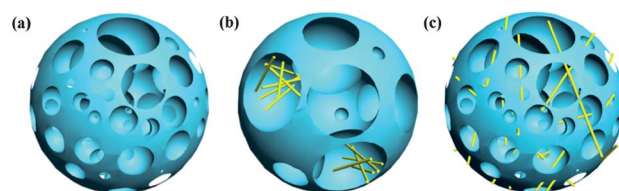
**Fig. 1** SEM and TEM images of CNTs (a, b and e) and N-CNTs (c, d and f).

diameter around 50 nm. The TEM images (Fig. 1e and f) illustrate that commercial CNTs have tubular morphology, while N-CNTs exhibit bamboo-like structure derived from N atoms doping. The N content was determined as 5.2 at% based on previous work.<sup>25</sup>

Elemental maps from N-CNTs were obtained by EDX spectroscopy on the SEM (Fig. 2). The instrument was able to detect traces of nitrogen in the N-doped case. It is clear that both carbon and nitrogen are present in the N-CNTs. Nitrogen is uniformly dispersed in the N-CNTs. Raman spectra of CNTs and N-CNTs are shown in Fig. 2d. The strong peaks at 1348 and 1584  $\text{cm}^{-1}$  are assigned to D-band and G-band, respectively. The G-band stands for the presence of graphite carbon, whereas D-band is attributed to disorders or defects in the graphite structure.<sup>27</sup> The intensity ratio of D and G bands ( $I_D/I_G$ ) is used to evaluate the disorder in the materials. The ratios  $I_D/I_G$  of CNTs and N-CNTs are 0.53 and 0.85, respectively. The higher  $I_D/I_G$  ratio implies more defects in N-CNTs.

The modified LFP composites were obtained by adding the dispersed CNTs and N-CNTs into the precursor. Final products were collected by the calcination process. As illustrated in Scheme 1, the interconnected pores are formed from vigorous gas evolution (mainly CO and CO<sub>2</sub>) during degradation of a citrate precursor. The interlacing LFP pores can serve as the channel for the penetration of the electrolyte through the electrode. Both CNTs and N-CNTs incorporate into the bulk porous network, leading to improved electrochemical performance. The dispersion of commercial CNTs in the porous structure is not homogeneous; in contrast, highly dispersed N-CNTs act as a bridge to connect all pores together for fast electrons transfer.

The phase composition for the as-obtained product has been identified with the X-ray diffraction (XRD) method, as demonstrated in Fig. 3. The majority of diffraction lines can be indexed to the orthorhombic phase LiFePO<sub>4</sub> (JCPDS no. 40-1499). The profiles of the reflection peaks are quite narrow, indicating the high crystallinity of the LFP samples. It also reveals that the addition of CNTs and N-CNTs has no effects on the main structure and the formation of LFP. It is noted that very small amount of impurity phases are also present in all samples, which



**Scheme 1** Schematic image of (a) porous LiFePO<sub>4</sub>; (b) LiFePO<sub>4</sub>/CNTs network and (c) LiFePO<sub>4</sub>/N-CNTs composites.

can be identified as Fe<sub>7</sub>(PO<sub>4</sub>)<sub>6</sub>. The minor impurity may appear under the reducing environment during the annealing process.<sup>28,29</sup>

Porous LFP was formed during the calcination process. SEM micrographs reveal a porous structure of the pristine LFP (Fig. 4a). Higher magnification image reveals the presence of numerous sub-micro sized apertures, these small apertures lead into much larger voids inside the particles, indicating the interior pore system is interlaced (Fig. 4b). The cross-sectional image of the cracked particle (see details in Fig. S1†) reveals that numerous micropores were distributed throughout the interior of the LFP particles, constructing a 3D interconnected pore system. Porous LFP/CNTs and LFP/N-CNTs composites are shown in Fig. 4c and e. The 3D CNT and N-CNT networks do not change the structure of the pristine porous LFP, but the degree of pore size uniformity is different, as shown in the lower magnification images. The distribution of pore sizes in LFP/N-CNTs is more homogeneous than that of CNTs, indicating that N-CNTs may regulate and control the uniform porous structure of LFP, which can be attributed to the uniform dispersion of the N-CNTs network. From high-resolution SEM images, the interlaced N-CNTs networks were uniformly incorporated into porous LFP particles, while CNTs were only located in certain big pores (dot dash line squared regions). The EDS elemental mapping for LFP/N-CNTs shows a uniform distribution of N, C, Fe, P and O (see ESI†, Fig. S2). The poor dispersion of the CNTs network restricts the formation of the homogeneous pore sizes in LFP during the calcination process and brings the nonuniform

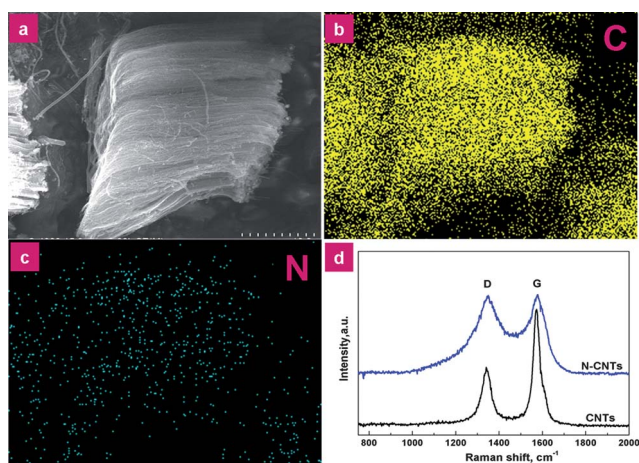


**Fig. 2** EDX elemental mappings (a, b and c) and Raman spectra (d) for N-CNTs.

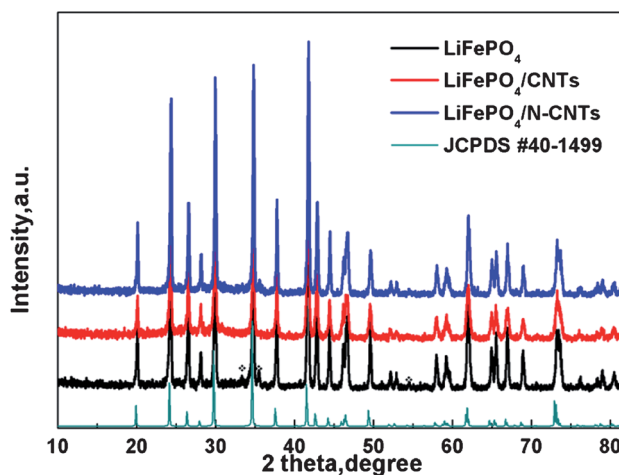


**Fig. 3** Powder X-ray diffraction patterns for porous LiFePO<sub>4</sub> and LiFePO<sub>4</sub> composite. \* represents the impurity phase.

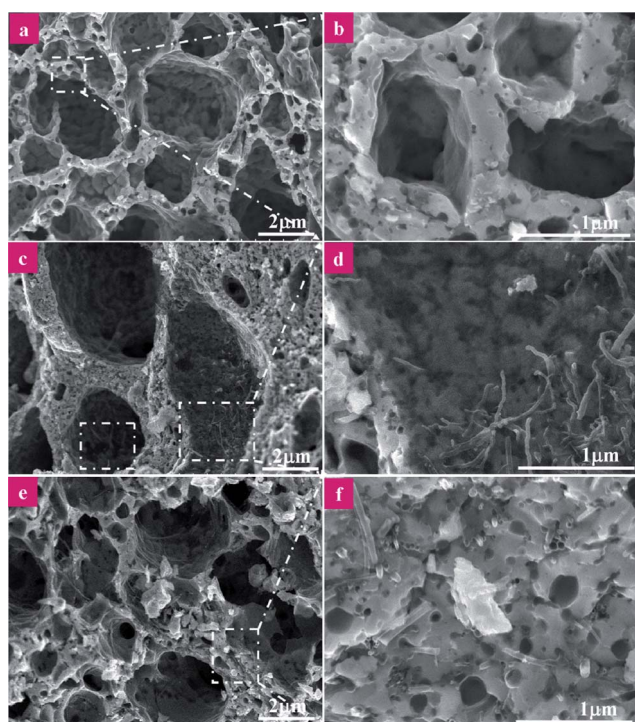


**Fig. 4** SEM images of (a and b) porous  $\text{LiFePO}_4$ ; (c and d)  $\text{LiFePO}_4/\text{CNTs}$  composite and (e and f)  $\text{LiFePO}_4/\text{N-CNTs}$  composite.

electron distribution. The specific BET surface area of the LFP/N-CNTs is  $11.6 \text{ m}^2 \text{ g}^{-1}$  and the pore diameter is around 90 nm. For LFP/CNTs and LFP, the surface area is 6.4 and  $2.3 \text{ m}^2 \text{ g}^{-1}$ , respectively. The incorporation of N-CNTs can greatly enhance the surface area of LFP, favouring the diffusion kinetics of lithium ions.

The Raman spectra of the pristine LFP and the modified composites are shown in Fig. 5a. Intense Raman modes were all observed at 216, 282, 393, 441, 987 and  $1078 \text{ cm}^{-1}$  in these three samples, which correspond to the finger print peaks of orthorhombic symmetry  $\text{LiFePO}_4$ .<sup>30</sup> Corresponding to the XRD results, the addition of CNTs and N-CNTs has no effects on the main structure of LFP. Carbon lines that appeared at pristine LFP are due to residual carbon from the decomposition of citrate. The  $I_D/I_G$  ratio for pristine LFP is calculated to be 4.97, indicating the large amount of amorphous carbon in the pristine LFP, which delivers low contribution to the electronic conductivity of the cathode material.<sup>31</sup> For modified composites, the  $I_D/I_G$  ratios are 0.55 and 0.95, respectively. The higher  $I_D/I_G$  ratio of N-CNTs indicated higher defectiveness, manifesting more defects in N-CNTs than CNTs.

To confirm the carbon content of the LFP and the modified composites, the thermal gravimetric analysis (TGA) was performed on LFP composites. Fig. 5b compares the TG curves of LFP *versus* the modified composites. According to the TG curves of LFP composites in air, at low temperature around  $230 \text{ }^\circ\text{C}$ , the weight loss is related to the absorbed moisture, then two reactions happen in the range of  $340 \text{ }^\circ\text{C}$  to  $550 \text{ }^\circ\text{C}$ , as previously reported, one is the oxidation of  $\text{LiFePO}_4$  to  $\text{Li}_3\text{Fe}_2(\text{PO}_4)_3$  and  $\text{Fe}_2\text{O}_3$ , which resulted in a weight gain of 5%<sup>32,33</sup> and the other is the combustion of the carbon to  $\text{CO}_2$ . It is noted that a plateau

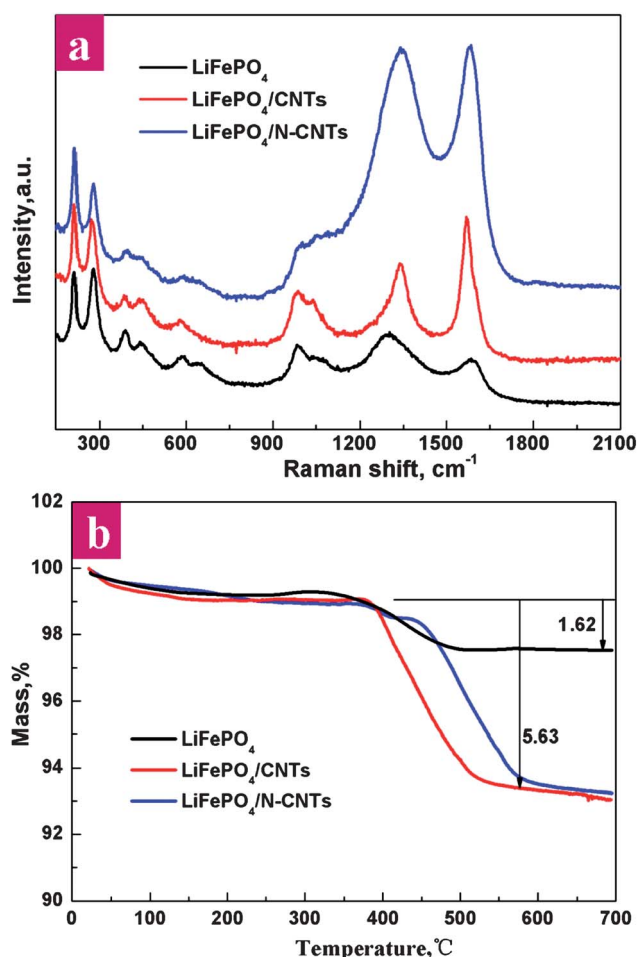


**Fig. 5** Raman spectra (a) and TGA curves (b) of the as-synthesized porous  $\text{LiFePO}_4$  and  $\text{LiFePO}_4$  composite.

appeared at about  $400 \text{ }^\circ\text{C}$ , indicating that the mass of the sample remains constant, which is due to the loss of the weight from the oxidation of carbon compared to the gain of weight from the formation of  $\text{Fe(III)}$ . The total weight loss for LFP in the TG curve is 1.62%, therefore the carbon content of LFP is 6.62 wt% (1.62 wt% + 5 wt%). For the modified composites, the incorporated CNTs and N-CNTs contributed to the increased carbon amount. Due to the same addition, the carbon content is 10.63 wt% (5.63 wt% + 5 wt%) for both composites.

Fig. 6 exhibits electrochemical performance for the pristine LFP and modified composites. Fig. 6a shows the charge and discharge curves of LFP, LFP/CNTs and LFP/N-CNTs at a constant current density of  $17 \text{ mA g}^{-1}$  for the 1<sup>st</sup>, 10<sup>th</sup> and 50<sup>th</sup> cycles. The initial profiles for all three samples exhibit a flat voltage plateau at around 3.4 V (*versus*  $\text{Li}^+/\text{Li}$ ), which is resulted from the two-phase redox reaction between  $\text{FePO}_4$  and  $\text{LiFePO}_4$ .<sup>6</sup> From the initial cycle of LFP/N-CNTs, the charge capacity is  $137 \text{ mA h g}^{-1}$  and the discharge capacity is  $119 \text{ mA h g}^{-1}$ , demonstrating the columbic efficiency is 87%, while 80% and 77% for LFP/CNTs and LFP, respectively. According to our testing results, the electronic conductivity for the LFP/N-CNTs can reach  $105 \text{ S m}^{-1}$ , while the electronic conductivity values for LFP/CNTs and LFP are 40 and  $10 \text{ S m}^{-1}$ , respectively. Therefore, the higher columbic efficiency of LFP/N-CNTs can be

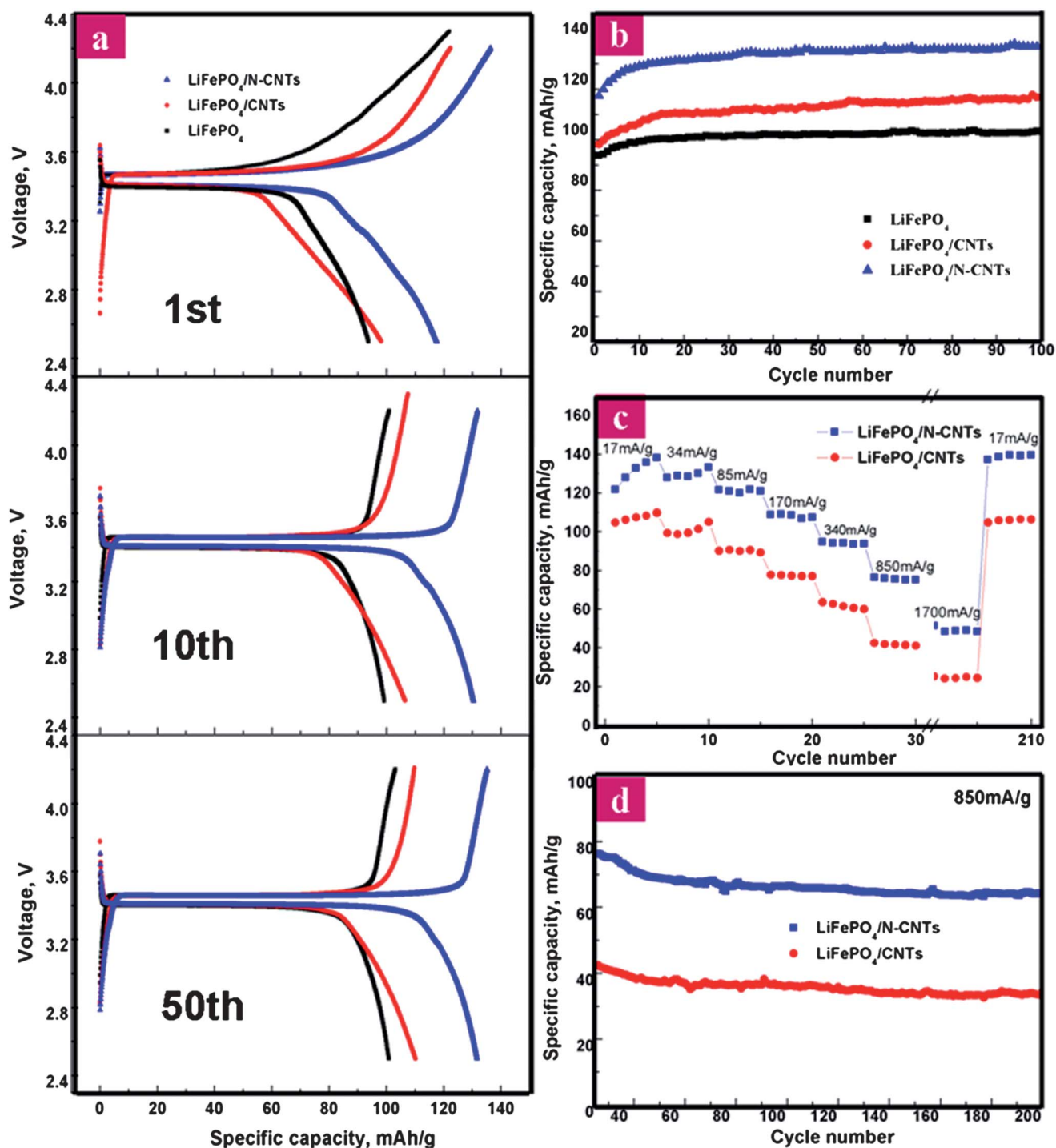


**Fig. 6** (a) Charge–discharge profiles of porous  $\text{LiFePO}_4$ ,  $\text{LiFePO}_4/\text{CNTs}$  and  $\text{LiFePO}_4/\text{N-CNTs}$  cycled at a current rate of 17 mA g<sup>-1</sup>; (b) discharge capacities during continuous cycling of lithium ion batteries at 17 mA g<sup>-1</sup>; (c) rate performance and (d) cycle performance of  $\text{LiFePO}_4/\text{CNTs}$  and  $\text{LiFePO}_4/\text{N-CNTs}$  cycled at a current rate of 850 mA g<sup>-1</sup>.

partially attributed to higher conductivity of the composites. Besides, the 3D network provided by the incorporated N-CNTs into LFP can increase the electrons and lithium ion diffusion rate, contributing to higher coulombic efficiency. On the subsequent cycling, such as in 10<sup>th</sup> and 50<sup>th</sup> cycles, the charge/discharge efficiency is close to 100% and the capacity retention is excellent. The voltage profiles of all three samples show a narrow gap

between charge and discharge, indicating low electrode resistance. The narrower the gap, the lower the electrode resistance is. From these three cycles (1<sup>st</sup>, 10<sup>th</sup> and 50<sup>th</sup>), the LFP/N-CNTs show narrower gap than the other two, indicating lower electrode resistance of the composite, which is in accordance with the conductivity testing results. In addition, the polarization between the charge and discharge curves of the modified LFP composites

is less than the pristine porous LFP, since the electrochemical conductivity of LFP is enhanced by addition of CNTs and N-CNTs. Closer examination of the curves shows that the polarization of LFP/N-CNTs is less than that of LFP-CNTs composites because nitrogen can induce defects to lower the activation energy for Li<sup>+</sup> diffusion, thus increasing the Li<sup>+</sup> diffusion rate.<sup>34</sup> For this reason, take the 50<sup>th</sup> cycle for example, LFP/N-CNTs composites exhibit a discharge capacity of 138 mA h g<sup>-1</sup> at a current rate of 17 mA g<sup>-1</sup>, while pristine porous LFP and LFP/CNTs composites display a discharge capacity of 104 and 113 mA h g<sup>-1</sup>, respectively.

In order to examine the cycle life of porous LFP and modified composites, long term discharge cycling at 17 mA g<sup>-1</sup> is performed, as shown in Fig. 6b. After 100 cycles, N-CNTs and CNTs modified composites still delivers the capacities of 138 and 113 mA h g<sup>-1</sup> respectively, while the pristine porous LFP displays a capacity of 104 mA h g<sup>-1</sup>, indicating that the incorporated N-CNTs and CNTs drastically enhance the specific capacity. The explanation is as follows: the 3D network of the CNTs and N-CNTs combined with the porous LFP particles increases the electrons and lithium ion diffusion rate. More importantly, unique cross-linked CNTs and N-CNTs facilitate electrons and lithium ion transfer in the inert zones, leading to high specific capacity. Moreover, the higher electronic conductivity of N-CNTs also improves the lithium ion and electrons diffusion rate, contributing to higher specific capacity of LFP/N-CNTs.<sup>24</sup> In addition, more uniform dispersion of N-CNTs into the porous network also provides more sufficient electronic conduction, leading to higher specific capacity of LFP. A recent report from Shao-horn's group indicated that functionalized CNTs could act as a cathode to store some lithium ions and deliver a reversible capacity.<sup>35</sup> In this case, N-CNTs might contribute some capacity as well. Meanwhile, our group is working on the effect of nitrogen on the electrochemical performance of electrode materials for LIBs,<sup>36</sup> which proved that nitrogen doping may improve the capacity in CNTs.

The comparison of rate performance for the LFP and the modified samples at different current densities from 17 mA g<sup>-1</sup> to 1700 mA g<sup>-1</sup> is shown in Fig. 6c. Under all charge/discharge rates, the discharge capacities of LFP/N-CNTs are higher than those of LFP/CNTs, highlighting N-CNTs modification is better than that of CNTs. It is noted that at high rates, such as 1700 mA g<sup>-1</sup>, the discharge capacity for LFP/N-CNTs composites still remains stable, but the capacity of LFP/CNTs fades significantly even at a lower rate of 340 mA g<sup>-1</sup>. Under high current density of 850 mA g<sup>-1</sup>, as shown in Fig. 6d, after 200 cycles, the LFP/N-CNTs still delivers a capacity of 68 mA h g<sup>-1</sup>, which is twice that of LFP/CNTs. As the observation from the above SEM images, more uniformly dispersed N-CNTs into the porous networks and inherent higher electronic conductivity facilitate the lithium ions and electrons diffusion, resulting in the excellent electrochemical performance at high-rate cycling. Another important feature is that as long as the current rate reverses back to a low current density of 17 mA g<sup>-1</sup>, the discharge capacity can recover to the original value for both modified samples, demonstrating that our 3D porous architecture is tolerant to varied charge and discharge currents, which is a highly desirable property required for lithium ion batteries applied in hybrid vehicle and electric vehicle markets.

## 4. Conclusions

In summary, 3D LFP/N-CNTs with hierarchical structure can be fabricated by a two-step process, sol-gel and calcination. Interpenetrating conductive N-CNTs and CNTs networks in the porous composites play the role of electron transport path in LFP. In comparison with LFP/CNTs, LFP/N-CNTs composites present higher specific capacity and excellent rate performance, which results from the improved lithium ions and electrons accessibility provided by the well dispersed N-CNTs in the porous LFP network and inherent superior electronic conductivity of N-CNTs. Our results demonstrated that LFP/N-CNTs is a promising cathode material for lithium ion batteries. This novel strategy can be extended to other cathode (or anode) materials of advanced batteries applied in electric vehicles.

## Acknowledgements

This work is supported by Natural Sciences and Engineering Research Council of Canada (NSERC), Phostech Lithium Inc., Canada Research Chair (CRC) Program and the University of Western Ontario. The authors express their sincere thanks to Dr Henry Huang for their kind help and discussions.

## Notes and references

- 1 P. G. Bruce, B. Scrosati and J.-M. Tarascon, *Angew. Chem., Int. Ed.*, 2008, **47**, 2930.
- 2 M. Armand and J.-M. Tarascon, *Nature*, 2008, **451**, 652.
- 3 K. Saravanan, M. V. Reddy, P. Balaya, H. Gong, B. V. R. Chowdari and J. J. Vittal, *J. Mater. Chem.*, 2009, **19**, 605.
- 4 Y. S. Hu, Y. G. Guo, R. Dominko, M. Gaberscek, J. Jamnik and J. Maier, *Adv. Mater.*, 2007, **19**, 1963.
- 5 L.-F. Cui, R. Ruffo, C. K. Chan, H. Peng and Y. Cui, *Nano Lett.*, 2009, **9**, 491.
- 6 A. K. Padhi, K. S. Nanjundaswamy and J. B. Goodenough, *J. Electrochem. Soc.*, 1997, **144**, 1188.
- 7 A. S. Andersson, J. O. Thomas, B. Kalska and L. Haggstrom, *Electrochem. Solid-State Lett.*, 2000, **3**, 66.
- 8 J. Wang and X. Sun, *Energy Environ. Sci.*, 2012, **5**, 5163.
- 9 B. Kang and G. Ceder, *Nature*, 2009, **458**, 190.
- 10 A. V. Murugan, T. Muraliganth and A. Manthiram, *Electrochem. Commun.*, 2008, **10**, 903.
- 11 P. S. Herle, B. Ellis, N. Coombs and L. F. Nazar, *Nat. Mater.*, 2004, **3**, 147.
- 12 K. L. Harrison and A. Manthiram, *Inorg. Chem.*, 2011, **50**, 3613.
- 13 N. Ravet, J. B. Goodenough, S. Besner, M. Simoneau, P. Hovington and M. Armand, Abstract 127, 196th ECS, Honolulu, Hawaii, 1999, 17.
- 14 Y.-H. Huang and J. B. Goodenough, *Chem. Mater.*, 2008, **20**, 7237.
- 15 K. Zaghbi, J. Shim, A. Guerfi, P. Charest and K. A. Striebel, *Electrochem. Solid-State Lett.*, 2005, **8**, A207.
- 16 R. Dominko, M. Bele, J. M. Goupil, M. Gaberscek, M. Remskar, D. Hanzel, I. Arcon and J. Jamnik, *Chem. Mater.*, 2007, **19**, 2960.
- 17 C. A. J. Fisher, V. M. Hart Prieto and M. S. Islam, *Chem. Mater.*, 2008, **20**, 5907.
- 18 J. Liu, M. Kunz, K. Chen, N. Tamura and T. J. Richardson, *J. Phys. Chem. Lett.*, 2010, **1**, 2120.
- 19 F. Yu, J. Zhang, Y. Yang and G. Song, *J. Power Sources*, 2009, **189**, 794.
- 20 S. W. Oh, S.-T. Myung, S.-M. Oh, K. H. Oh, K. Amine, B. Scrosati and Y.-K. Sun, *Adv. Mater.*, 2010, **22**, 4842.
- 21 S. W. Oh, S.-T. Myung, H. J. Bang, C. S. Yoon, K. Amine and Y.-K. Sun, *Electrochem. Solid-State Lett.*, 2009, **12**, 181.
- 22 C. M. Doherty, R. A. Caruso, B. M. Smarsly, P. Adelhelm and C. J. Drummond, *Chem. Mater.*, 2009, **21**, 5300.
- 23 Y. Zhou, J. Wang, Y. Hu, R. O'Hayreb and Z. Shao, *Chem. Commun.*, 2010, **46**, 7151.

- 
- 24 H. Liu, Y. Zhang, R. Li, X. Sun, D. Désilets and H. Abou-Rachid, *Carbon*, 2010, **48**, 1498.
- 25 J. Liu, Y. Zhang, M. Ionescu, R. Li and X. Sun, *Appl. Surf. Sci.*, 2011, **257**, 7837.
- 26 Y. T. Lee, N. S. Kim, S. Y. Bae, S. C. Yu, H. Ryu, H. J. Lee and J. Park, *J. Phys. Chem. B*, 2003, **107**, 12958.
- 27 H. Hiura, T. W. Ebbesen, K. Tanigaki and H. Takahashi, *Chem. Phys. Lett.*, 1993, **202**, 509.
- 28 A. A. Salah, A. Mauger, C. M. Julien and F. Gendron, *Mater. Sci. Eng., B*, 2006, **129**, 232.
- 29 S. P. Ong, L. Wang, B. Kang and G. Ceder, *Chem. Mater.*, 2008, **20**, 1799.
- 30 A. A. Salah, A. Mauger and K. Zaghbi, *J. Electrochem. Soc.*, 2006, **153**, 1692.
- 31 M. M. Doeff, J. D. Wilcox, R. Kostecki and G. Lau, *J. Power Sources*, 2006, **163**, 180.
- 32 I. Belharouak, C. Johnson and K. Amine, *Electrochem. Commun.*, 2005, **7**, 983.
- 33 X. Lou and Y. Zhang, *J. Mater. Chem.*, 2011, **21**, 4156.
- 34 Z. Liu, X. Huang and D. Wang, *Solid State Commun.*, 2008, **147**, 505.
- 35 S. W. Lee, N. Yabuuchi, B. M. Gallant, S. Chen, B. S. Kim, P. T. Hammond and Y. S. Horn, *Nat. Nanotechnol.*, 2010, **5**, 531.
- 36 X. Li, J. Liu, Y. Zhang, Y. Li, H. Liu, X. Meng, J. Yang, D. Geng, D. Wang, R. Li and X. Sun, *J. Power Sources*, 2012, **197**, 238.